The impact of radial electric fields and plasma rotation on intermittence in TJ-II

B.Ph. van Milligen[1], B.A. Carreras[2,3], L. García[2], G. Grenfell[4], I. Voldiner[1], C. Hidalgo[1] and the TJ-II Team‡

[1] National Fusion Laboratory, Centro de Investigaciones Energéticas, Medioambientales y Tecnológicas, Avda. Complutense 40, 28040 Madrid, Spain
[2] Departamento de Física, Universidad Carlos III de Madrid, Avda. de la Universidad 30, 28911 Leganes, Madrid, Spain
[3] Department of Physics, University of Alaska, Fairbanks, AK 99775-5920, USA
[4] Max Planck Institute of Plasma Physics, Boltzmannstraße 2, 85748 Garching bei München, Germany

Abstract. This work explores the impact of an imposed radial electric field on the intermittence parameter in magnetically confined plasmas. The intermittence is sensitive to both the magnetic configuration (dominant helical modes or low order rational surfaces) and to poloidal flows or radial electric fields. This behaviour was verified both in numerical turbulence calculations using a resistive MHD model and using Langmuir probe data obtained in experiments at the TJ-II stellarator. It is shown that the intermittence parameter can be used to detect when the local plasma rotation velocity with respect to the laboratory frame of reference is minimum.

‡ ORCID codes: B.Ph. van Milligen: 0000-0001-5344-6274; B.A. Carreras: 0000-0001-7921-4690; L. García: 0000-0002-0492-7466; G. Grenfell: 0000-0003-0107-5787; I. Voldiner: 0000-0001-6703-7754

1. Introduction

Turbulence tends to carry a significant fraction of the radial transport of particles and heat in magnetically confined plasmas [1]. The radial transport in turn determines the economic viability of putative future fusion reactors for energy production based on the concept of magnetic confinement. Hence, advancing our understanding of turbulence in fusion plasmas is both urgent and important.

An important aspect of turbulence is intermittence. Intermittence involves the alternation of periods with different fluctuation amplitudes, such as steady turbulence interrupted by occasional large amplitude bursts [2]. These bursts can sometimes be associated with relaxation events occurring in the strongly driven fusion plasma, also denoted 'streamers' or 'avalanches'. To quantify this behaviour, we make use of a method originating in chaos theory [3]. The corresponding intermittence parameter, $C(1)$, is a quantifier of the degree of multifractality of a measured signal, such that a monofractal signal yields $C(1) = 0$ and a multifractal signal $0 < C(1) \leq 1$.

Perhaps somewhat unexpectedly, previous work [4] has shown that $C(1)$ turns out to be very useful in the framework of the study of the interaction between turbulence, low order rational surfaces and plasma flows in fusion plasmas. It is well known that fluctuations may be driven by the presence of thermodynamic gradients. Fluctuations near a low order rational surface may be dominated by the turbulent structure of the resonant helicity ('filaments'). When fluctuations are dominated by such a single mode, the fluctuations will tend to be monofractal in nature, resulting in $C(1) \simeq 0$.

The mixing of fluctuations from various sources may raise $C(1)$ due to increased multifractality. This can be the case when, at a given location, various helicities contribute to the fluctuations. Another situation that may raise $C(1)$ is the presence of a net poloidal flow velocity. The local temporal fluctuation structure of the turbulence can then get mixed with its poloidal structure, leading to enhanced multifractality. A radial variation (shear) in the mean poloidal flow would lead to a gradually varying value of $C(1)$ with radial position. In the cited work, we show that these properties imply that one can use the detected value of $C(1)$ as a means to locate the low order rational surfaces, which tend to coincide with local minima of $C(1)$. It was also seen that the presence of a radial electric field (often equivalent to a poloidal flow) may modify this picture due to the mentioned temporal-spatial mixing.

To further clarify this issue, in the present work, we study the impact of a radial electric field on the intermittence parameter $C(1)$ in a systematic way. For this purpose, we make use of TJ-II discharges in which an external electric field was applied by means of a biased electrode inserted into the plasma.

This article is organized as follows. Section 2 discusses the methods we have used for data analysis and the numerical model for simulation of turbulence. Section 3 presents some simulations performed using a resistive MHD turbulence model. Section 4 presents the experimental results. In Section 5 we discuss the results and draw some conclusions.

2. Methods

The experiments discussed here have been performed at TJ-II, a flexible Heliac [5]. with toroidal magnetic field $B_T \simeq 1$ T, major radius $R_0 = 1.5$ m and minor radius $a < 0.22$ m [6]. Plasmas can be heated using two Electron Cyclotron Resonance Heating (ECRH) beam lines delivering up to 300 kW each at a frequency of 53.2 GHz (X mode) and two Neutral Beam Injector (NBI) systems (co and counter) with up to 2×700 kW port-through power.

The experiments were performed using the standard magnetic configuration of TJ-II, which has an edge rotational transform close to 1.65 (such that the $n/m = 8/5$ rational surface is located at $\rho \simeq 0.76$). The hydrogen plasmas were heated initially by ECRH and subsequently sustained by NBI heating. The reported results were obtained using NBI co-injection with $P_{NBI} \simeq 500$ kW.

In this section, we briefly describe the tools we used in this study. Section 2.1 describes the probe systems we used. Section 2.2 describes the calculation of the intermittency parameter, $C(1)$. Section 2.3 describes the resistive MHD model used to perform the turbulence calculations.

2.1. Probe systems

TJ-II is fitted with two reciprocating Langmuir probe drives, located at toroidal angles $\phi = 38.2°$ (the D probe, entering the plasma from above) and $\phi = 195°$ (the B probe, entering the plasma from below). Each drive can be fitted with different probe heads. In the experiments discussed here, the D probe was fitted with a two-dimensional probe head (with 4×5 pins laid out in a poloidal-radial grid), while the B probe was fitted with a rake probe (with 12 pins laid out in a radial array). For more details, please refer to [7].

TJ-II also disposes of a 2-D carbon composite mushroom-shaped electrode (12 mm high, with a diameter of 25 mm), installed on a fast reciprocating probe drive at $\phi = 174.4°$, entering from above. The electrode was inserted about 2 cm inside the last closed flux surface (LCFS), to $\rho \simeq 0.85$, and biased with respect to one of the two TJ-II limiters [8].

2.2. Intermittency

In this article, we use the method for calculating the intermittence of temporal signals described in Refs. [9, 10, 11], which we summarize here for convenience. Given a time series $X = \{x_i, i = 1, \ldots, N\}$ that has been sampled at a constant sampling rate, we calculate the measure

$$\epsilon(1, i) = \frac{(x_i - \langle x_i \rangle)^2}{\langle (x_i - \langle x_i \rangle)^2 \rangle}, \qquad i = 1, \ldots, N, \tag{1}$$

where $\langle x_i \rangle = (\sum_{i=1}^{N} x_i)/N$. This measure can be averaged over subblocks of data of

length $n < N$, as follows:

$$\epsilon(n,i) = \frac{1}{n}\sum_{j=0}^{n-1}\epsilon(1,i+j). \tag{2}$$

We then calculate the $\mathbb{q}$-moments, $\langle\epsilon(n,i)^{\mathbb{q}}\rangle$. In a given range of n-values, these moments are expected to scale like [12]:

$$\langle\epsilon(n,i)^{\mathbb{q}}\rangle \propto n^{-K(\mathbb{q})}, \tag{3}$$

where $K(1) \equiv 0$. If the time series X is monofractal, the function $K(\mathbb{q})$ is asymptotically linear in $\mathbb{q}$, otherwise the series is multifractal. The parameter $C(\mathbb{q})$ is defined as [12]:

$$C(\mathbb{q}) = \frac{K(\mathbb{q})}{\mathbb{q}-1} \tag{4}$$

and is related to the so-called generalized dimension $D(\mathbb{q}) = 1 - C(\mathbb{q})$. Of special interest is the so-called "intermittency parameter" $C(1)$, which must be calculated as

$$C(1) = \left.\frac{dK(\mathbb{q})}{d\mathbb{q}}\right|_{\mathbb{q}=1} \tag{5}$$

due to the singularity of Eq. 4 at $\mathbb{q} = 1$. Its value ranges from 0, for a monofractal time series, to 1. Details of the calculation of $C(1)$ are given in [11], and the robustness of this parameter with respect to experimental noise is discussed in [13].

In the past, intermittence has often been characterized using the fact that intermittence ('burstiness') tends to increase the kurtosis of the corresponding time series [14]. It can be shown that the present quantifier is superior, based on the fact that it considers the temporal variations of a signal rather than merely the shape of its probability distribution.

As noted in the introduction, the intermittence (or degree of multifractality $C(1)$) provides valuable information about the nature of turbulence. At locations where a single unstable mode dominates, the degree of multifractality will be low. In the case of magneto-hydrodynamic (MHD) turbulence, the unstable (helical) modes are associated with rational surfaces, although their mode amplitude may peak off the rational surface location, depending on the symmetry of the eigenmode [4]. Multifractality may increase when several modes overlap (due to, e.g., a high density of unstable rational surfaces). It also increases due to poloidal plasma flow, as that leads to a mixing between the temporal and spatial (poloidal) structure of a given mode for measurements taken at a fixed point.

2.3. Resistive MHD model

The model used for the present calculations is a resistive MHD turbulence model which has been used in the past to interpret some experimental results from the TJ-II [15, 16] and W7-X [17] stellarators. It is based on the reduced MHD equations [18], the dominant instability being pressure gradient modes. The geometry is that of a periodic cylinder, with minor radius a and length $L = 2\pi R_0$. We use a coordinate system (r, θ, ζ),

in which r is the radius of the cylindrical surface, θ is the poloidal angle, and $\zeta = z/R_0$, where z is the coordinate along the axis of the cylinder, so ζ is an effective toroidal angle when the cylinder is bent in a torus.

The four equations of the model are summarized here in their dimensionless form,

$$\frac{\partial \tilde{\psi}}{\partial t} = \nabla_\parallel \Phi - S\bar{\omega}_{*e}\left(\frac{T_{eq}}{n_{eq}}\nabla_\parallel n + \nabla_\parallel T_e\right) + \eta \tilde{J}_\parallel, \tag{6}$$

$$\frac{\partial \tilde{U}}{\partial t} = -\mathbf{v}_\perp \cdot \nabla U + S^2 \nabla_\parallel J_\parallel - S^2 \frac{\beta_0}{2\varepsilon^2}\kappa\left(\frac{T_{eq}}{n_{eq}}\frac{1}{r}\frac{\partial \tilde{n}}{\partial \theta} + \frac{1}{r}\frac{\partial \tilde{T}_e}{\partial \theta}\right) + \mu \nabla_\perp^2 \tilde{U}, \tag{7}$$

$$\frac{\partial \tilde{n}}{\partial t} = -\mathbf{v}_\perp \cdot \nabla n + \frac{S}{\bar{\omega}_{ci}}\nabla_\parallel J_\parallel + D_\perp \nabla_\perp^2 \tilde{n}, \tag{8}$$

$$\frac{\partial \tilde{T}_e}{\partial t} = -\mathbf{v}_\perp \cdot \nabla T_e + \frac{S}{\bar{\omega}_{ci}}\frac{T_{eq}}{n_{eq}}\nabla_\parallel J_\parallel + \chi_\perp \nabla_\perp^2 \tilde{T}_e + \nabla_\parallel\left(\chi_\parallel \nabla_\parallel T_e\right). \tag{9}$$

The first equation, describing the evolution of the poloidal magnetic flux ψ, is derived from Faraday's and Ohm's laws. The second one is the momentum balance equation where U is the z component of the vorticity. The other two equations give the evolution of density n and electron temperature T_e. All the quantities appearing in equations (6)-(9) are decomposed in an equilibrium component f_{eq} and a fluctuating component $\tilde{f}$, so $f = f_{eq} + \tilde{f}$.

The electrostatic potential is Φ and the velocity stream function is $\phi = \Phi/B_z$. So the electric field is $\mathbf{E} = -\nabla\Phi$ and the perpendicular velocity is

$$\mathbf{v}_\perp = -\nabla\phi \times \mathbf{z}, \tag{10}$$

where $\mathbf{z}$ is the unit vector in the toroidal direction.

The parallel current density is $J_\parallel = \nabla_\perp^2 \psi$, and $U = \nabla_\perp^2 \Phi$. The resistivity is η, the viscosity is μ and the perpendicular diffusivity is $D_\perp$. $\chi_\parallel$ and $\chi_\perp$ are the parallel and perpendicular thermal diffusivity, respectively. β_0 is the ratio of the plasma pressure, p, and the magnetic pressure, $B_z^2/2\mu_0$, at the plasma axis: $\beta_0 = 2\mu_0 p(0)/B_z^2$, where B_z is the toroidal magnetic field and μ_0 is the vacuum permeability; τ_R is the resistive time at the magnetic axis, $\tau_R = \mu_0 a^2/\eta(0)$, where $\eta(0)$ is the resistivity at the magnetic axis and τ_A is the Alfvén time, $\tau_A = R_0\sqrt{\mu_0 m_i n_i}/B_z$, where m_i and n_i are the ion mass and density, respectively. R_0 and a are the major and minor radius, respectively, and the inverse aspect ratio is $\varepsilon = a/R_0$. The Lundquist number $S = \tau_R/\tau_A$. $\overline{\omega}_{*e} = \tau_A \omega_{*e}$, where $\omega_{*e} = T_e/ea^2 B_z$ is the electron diamagnetic frequency; $\overline{\omega}_{ci} = \tau_A \omega_{ci}$, where $\omega_{ci} = eB_z/m_i$ is the ion cyclotron frequency.

In the set of equations (6)–(9) density is normalized to $n_i(0)$, magnetic fields are normalized to B_z, lengths are normalized to minor radius a, and time to τ_R. The electron temperature and resistivity are normalized to their respective values at the magnetic axis. In the numerical calculations, $\varepsilon = 0.15$, $S = 2 \times 10^5$, $\beta_0 = 10^{-3}$, $\bar{\omega}_{*e} = 2 \times 10^{-4}$, $\bar{\omega}_{ci} = 500$. The diffusivity parameters used are $D_\perp = \chi_\perp = 0.1a^2/\tau_R$ and $\mu = 0.05a^2/\tau_R$. The parallel electron heat conductivity is $\chi_\parallel = 2 \times 10^6 R_0^2/\tau_R$.

The physical variables are decomposed in Fourier series for the poloidal and toroidal angle and the radial direction is solved using finite differences so

$$f\left(r,\theta,\zeta,t\right)=\sum_{m,n}\left[f_{m,n}^{s}\left(r,t\right)\sin\left(m\theta+n\zeta\right)+f_{m,n}^{c}\left(r,t\right)\cos\left(m\theta+n\zeta\right)\right]. \quad (11)$$

In the present numerical calculations we introduce the resonant helicities, corresponding to the rotational transform profile, up to $m = 100$ which give a total number of angular components of 446. The value $m = 100$ is chosen because it is a sufficiently high value of m so that the resistive interchange turbulence is saturated through dissipation. The finite difference grid consists of 400 unequally spaced points between $r = 0$ and $r = 0.5$ and 1000 equally spaced points between $r = 0.5$ and $r = 1$.

3. Numerical calculations

We use the Resistive MHD turbulence model to calculate turbulence for a TJ-II configuration (the 'standard' configuration, labelled 100_44) in steady state. Resistive pressure gradient driven instabilities are dominant. Once steady state was achieved, we imposed an additional constant electric field, E_{r0}, in the region $0.5 < r/a < 1.0$, which induces a constant poloidal rotation. The calculation was then continued to study the effect of this electric field on the turbulence. We have performed this calculation for five values of the electric field normalized to aB_z/τ_R : $-200, -100, 100, 200,$ and 300. For all these cases, we have evaluated the intermittence parameter for potential and electron temperature fluctuations. Near the rational surfaces, the corresponding resonant helicity is dominant, and in the absence of poloidal rotation the signal is monofractal and $C(1)$ is close to zero. As noted in the introduction, the effect of the poloidal rotation is to mix the intermittence due to temporal fluctuations with the one induced by the poloidal structure of the same fluctuations. This mixture increases the degree of the multifractality of the signal. Accordingly, the observed value of the intermittence parameter responds to the imposed $E_{r0}/B_z = -V_{\theta 0}$. This effect was most visible for the potential fluctuations (Φ), and somewhat less clear for electron temperature fluctuations (T_e).

Fig. 1 shows the intermittence parameter $C(1)$ (of the potential fluctuations, Φ) as a function of the radius for a small radial range and for the mentioned values of the imposed radial electric field E_{r0}. Near the 8/5 rational surface, the profile of $C(1)$ shows a clear minimum for $E_{r0} = -200\ aB_z/\tau_R$, which becomes less deep as E_{r0} increases. Around $E_{r0} = 200\ aB_z/\tau_R$ the minimum disappears.

Fig. 2 shows the variation of the intermittence parameter $C(1)$ (of the electron temperature fluctuations, T_e) as a function of the radius for a small radial range and for the different values of the imposed radial electric field E_{r0}. The minimum at the main low order rational surface, 8/5, is visible for all values of the applied radial electric field E_{r0}, although it is deeper for negative than for positive E_{r0}.

Fig. 3 shows the variation of the intermittence parameter $C(1)$ (of the potential fluctuations, Φ) as a function of the poloidal rotation $V_{\theta 0}$ imposed by the applied field E_{r0} at the location of the two lowest order rational surfaces in the calculation. Both curves show a minimum at a specific value of $V_{\theta 0}$. This suggests that the value of the rotation velocity at this minimum corresponds to the situation where the poloidal rotation imposed by the applied E_{r0} compensates the spontaneous rotation: at the 11/7 surface (located at $\rho \simeq 0.50$), the spontaneous rotation is therefore about 100 a/τ_R, and at the 8/5 surface (located at $\rho \simeq 0.76$), it is about -200 a/τ_R.

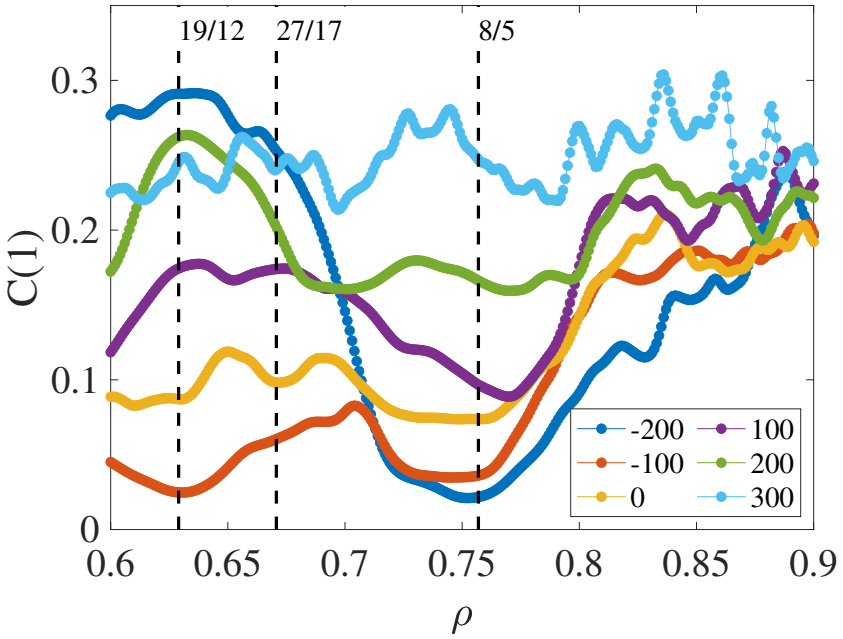

Figure 1. Intermittence parameter $C(1)$ of the potential fluctuations, Φ, as a function of the radius. The legend indicates the applied radial electric field E_{r0}, in units of aB_z/τ_R.

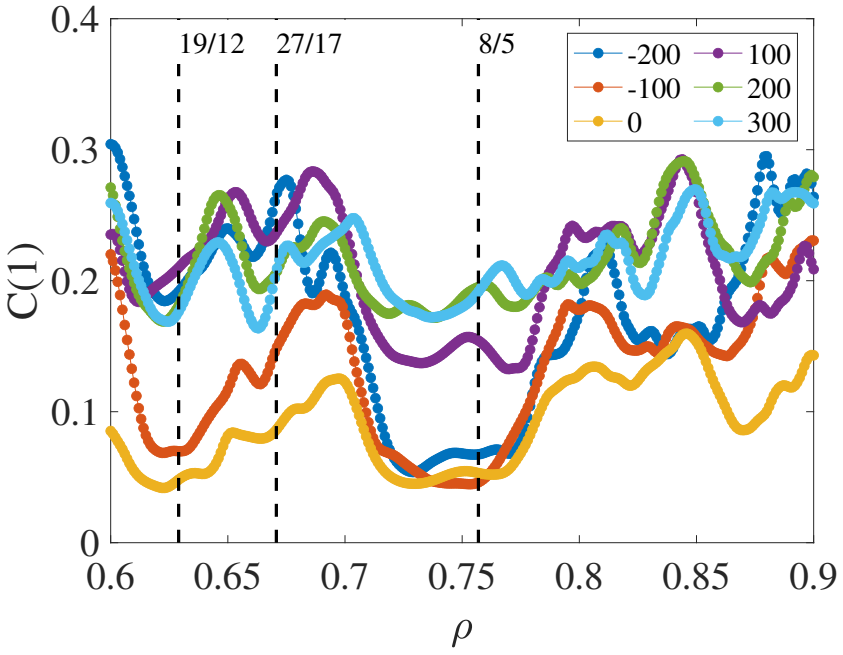

Figure 2. Intermittence parameter $C(1)$ of the electron temperature fluctuations, T_e as a function of the radius. The legend indicates the applied radial electric field E_{r0}, in units of aB_z/τ_R.

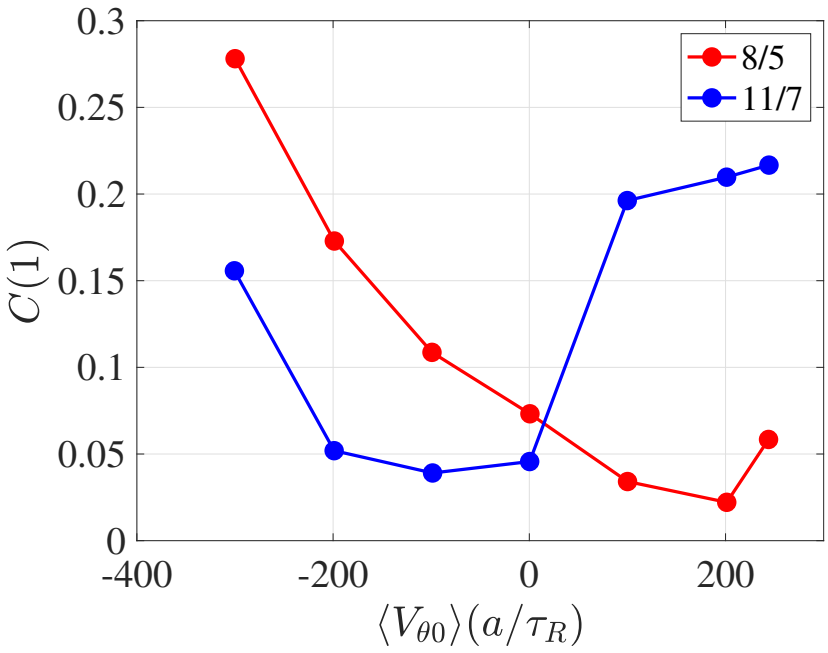

Figure 3. Intermittence parameter $C(1)$ of the potential fluctuations as a function of the poloidal rotation $V_{\theta 0}$ imposed by the applied electric field at two resonant positions.

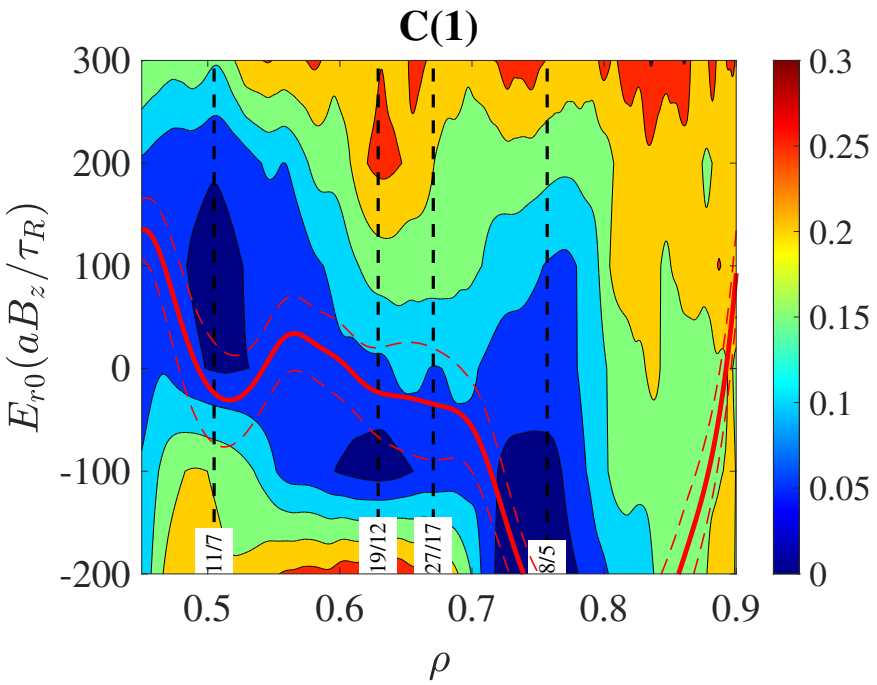

Figure 4. Intermittence parameter $C(1)$ of the potential fluctuations as a function of the imposed radial electric field E_{r0}. Vertical dashed lines indicate a few low order rational surfaces, as indicated by the corresponding labels. The thick red line is minus the spontaneous poloidal rotation ($+V_{\theta 0}B_z$ at $E_{r0} = 0$). Thin, dashed red lines indicate the corresponding error.

Fig. 4 shows the data of Fig. 1 in a two-dimensional representation. This figure clarifies that the deepest minima of $C(1)$ (dark blue) tend to occur at positions corresponding to low order rational surfaces. As noted, the minimum at a specific value of ρ occurs at the value of the imposed poloidal rotation velocity that compensates the spontaneous rotation. If one connects the minima of $C(1)$ at different ρ values, the background velocity rotation profile can therefore be recovered, in principle. To clarify this, we have superposed minus the profile of the spontaneous rotation (without applied field E_{r0}). It is seen that the values of E_{r0} where the minima occur approximately match the negative spontaneous rotation. In other words, $C(1)$ roughly attains its minimum when the rotation is halted with respect to the laboratory frame of reference.

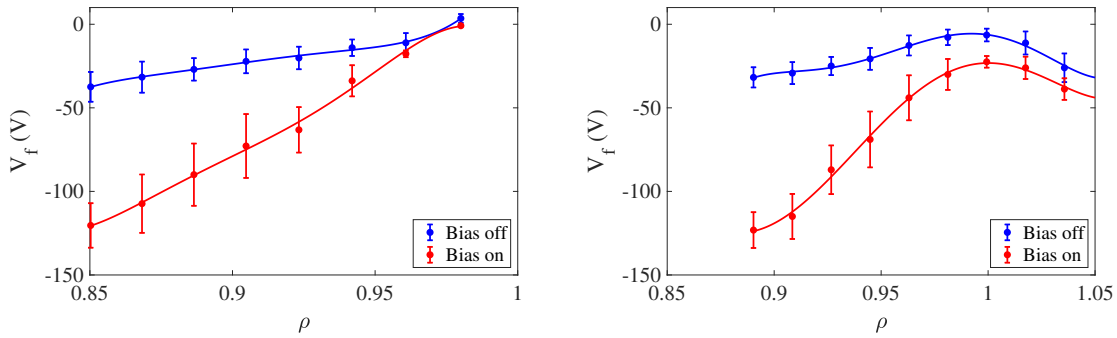

Figure 5. Floating potential profile, biasing on/off, NBI conditions. Left: D probe; right: B probe.

4. Experimental results

The following sections present the experimental results in two conditions: (a) NBI-heated high density plasmas (ion root, characterized by a negative radial electric field in the plasma edge region) and (b) ECR-heated low density plasmas (electron root, characterized by a positive radial electric field in the plasma edge region).

4.1. Ion root phase

The discharges analyzed here have been reported in detail in Ref. [19]. The main features of the plasmas have been summarized in Section 2. The electron density was fairly constant in the interval $1165 < t < 1240$ ms, corresponding to the NBI phase, with a value of $\overline{n_e} \simeq 1 \cdot 10^{19}$ m^{-3}. Central electron temperatures were in the range of $300 < T_e(0) < 400$ eV. The voltage applied to the biasing probe was a 40 Hz square wave with an amplitude of -350 V and a duty cycle of 50%. In each discharge, the Langmuir probes were moved to a slightly different radial position, allowing the reconstruction of profiles over a relatively wide radial range on a shot-by-shot basis.

We quantified the measurements by detecting the 'biasing on' and 'biasing off' time intervals; each time interval lasting 12.5 ms. We rejected the first 0.5 ms and the last 0.5 ms of each time interval to avoid transient effects, so each biasing phase yielded 11.5 ms of useful data. Over whole time window analyzed, we obtained 6 or 7 such time intervals, depending on the discharge. Fig. 5 shows the mean profile of the floating potential, averaged over the selected discharges and the biasing time intervals, for the two levels of biasing. The error bars indicate the standard deviation of values obtained for the various discharges and biasing time intervals.

Fig. 6 shows the profile of the intermittence parameter of the floating potential fluctuations, $C1(V_f)$, averaged over the selected discharges and the biasing time intervals, for the two levels of biasing.

Fig. 7 shows $-dV_f/d\rho$, calculated by fitting a 5$^{\text{th}}$ order polynomial to the profiles

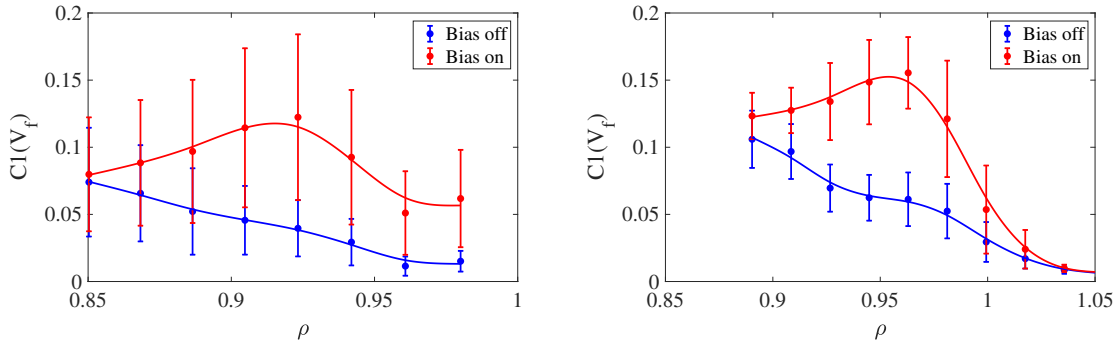

Figure 6. Intermittence parameter, $C(1)$, biasing on/off, NBI conditions. Left: D probe; right: B probe.

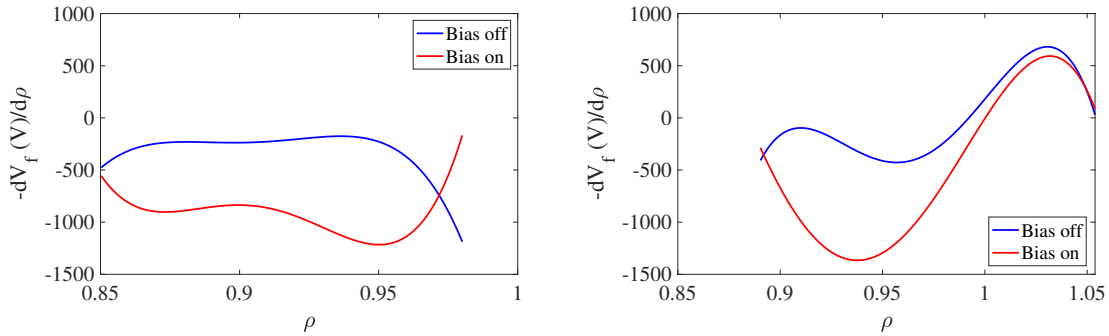

Figure 7. $-dV_f/d\rho$, biasing on/off, NBI conditions. Left: D probe; right: B probe.

of Fig. 5 (shown as continuous lines in that figure) and taking the derivative. This procedure is especially inaccurate near the edges of the data interval, so the apparent rapid changes seen for the smallest and largest values of ρ in each graph should be ignored. The quantity $-dV_f/d\rho$ is a proxy for the radial electric field $E_r = -dV_p/dr$ assuming electron temperature gradient effects are small, noting $d/dr \simeq (1/a)d/d\rho$ with $a \simeq 0.2$ m. Comparing biasing on and biasing off, one observes that $-dV_f/d\rho$ is generally more negative when biasing is on. In the case of the B probe, the position of the highest value of $|-dV_f/d\rho|$ (near $\rho = 0.95$) is seen to coincide approximately with the position of the highest values of $C(1)$. In the case of the D probe, resolution may not be sufficient to see this effect clearly.

In another set of experiments, the polarization voltage waveform was triangular. A single modulation period consisted of a linear ramp from 0 to -340 V in 6.25 ms, a linear ramp from -340 to 0 V in 6.25 ms, followed by a non-biasing interval (0 V) lasting 12.5 ms. Plasma conditions were similar as in the discharges reported above. The B probe was moved radially from one discharge to the next. To reconstruct the spatiotemporal evolution, data from 4 shots were combined by synchronizing (subtracting a reference

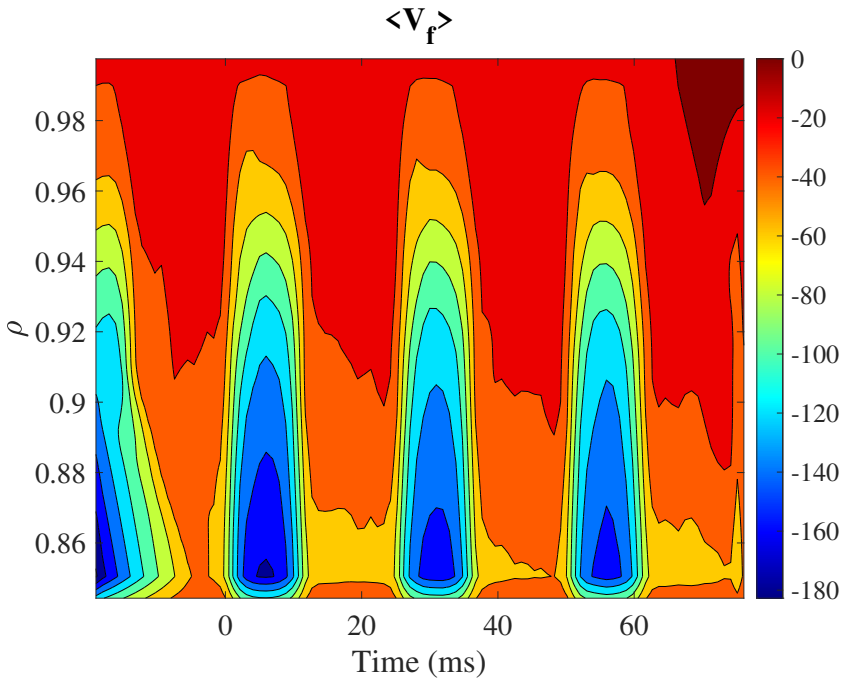

Figure 8. The mean evolution of V_f (V) vs. ρ and $t - t_0$ for 4 shots. Data from probe B.

time, t_0, corresponding to the start of a biasing ramp). Fig. 8 shows the evolution of the mean floating potential, V_f. Fig. 9 shows the corresponding intermittence, $C(1)$. When biasing is activated, $C(1)$ increases predominantly at $\rho \simeq 0.95$, corresponding to the location of the 18/11 rational and the location of highest $E_r \simeq -a^{-1} dV_f/d\rho$ (the radial region where the contours are closest together in Fig. 8). This matches the result shown in Fig. 6 for square wave biasing.

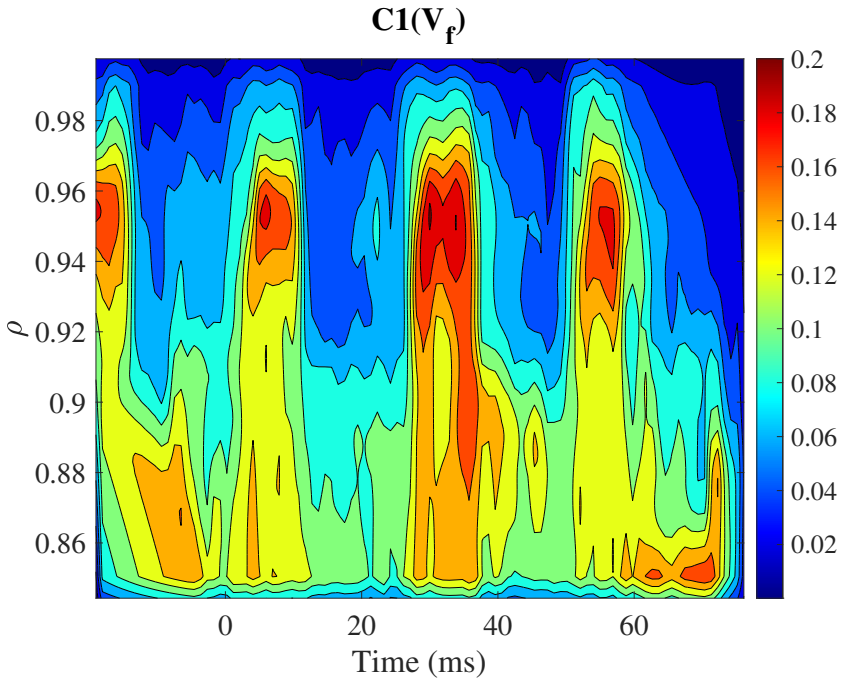

Figure 9. The mean evolution of $C(1)$ vs. ρ and $t - t_0$ for 4 shots. Data from probe B.

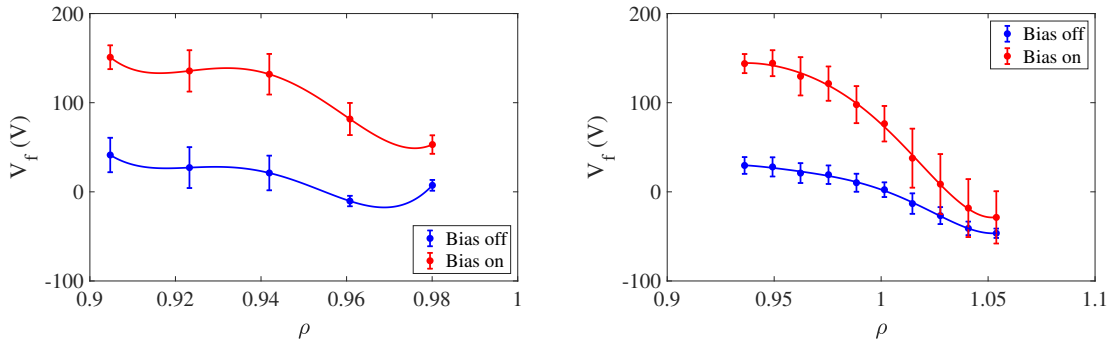

Figure 10. Floating potential profile, biasing on/off, ECRH conditions. Left: D probe; right: B probe.

4.2. Electron root phase

Similar experiments were performed in ECR-heated conditions, yielding lower electron densities such that the plasma was in the electron root state. In the relevant time window, the line average density was approximately $\overline{n_e} = 0.4 \cdot 10^{19}$ m^{-3}. Central electron temperatures were approximately $T_e(0) \simeq 1.5$ keV. Again, square wave biasing was applied, as described in Section 2. The applied biasing was a 40 Hz square wave signal alternating between 0 and +230 V in a duty cycle of 50%. The analysis is fully analogous to the procedure for the analysis of the square wave modulation described in the previous section.

Fig. 10 shows the mean profile of the floating potential, averaged over the selected discharges and the biasing time intervals, for the two levels of biasing. The error bars indicate the standard deviation of values obtained for the various discharges and biasing time intervals.

Fig. 11 shows the profile of the intermittence parameter of the floating potential fluctuations, $C1(V_f)$, averaged over the selected discharges and the biasing time intervals, for the two levels of biasing.

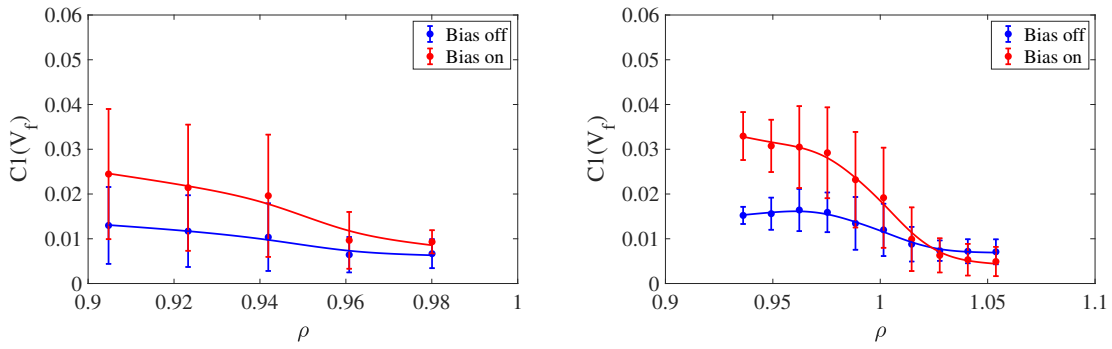

Figure 11. Intermittence parameter, $C(1)$, biasing on/off, ECRH conditions. Left: D probe; right: B probe.

5. Discussion and conclusions

In order to study the impact of a radial electric field on the intermittence, numerical simulations were performed using a resistive MHD turbulence code in which a constant radial electric field was added. It was observed that the intermittence responded to the imposed electric field. The variation of the intermittence due to the imposed electric field was largest near low order rational surfaces. The intermittence value was lowest when the imposed electric field compensated the spontaneously generated electric field.

To verify this behaviour in an experimental context, a biasing probe was used to significantly modify the plasma potential profile (and hence the radial electric field) in the edge region of the TJ-II stellarator. Specific biasing waveforms were used to facilitate the comparison between biasing on and biasing off phases. Experiments were performed in both ion and electron root conditions (high and low line average electron density, respectively).

In ion root conditions, biasing was such as to decrease the potential and to enhance the absolute value of the negative radial electric field, E_r. The enhancement of E_r was maximum around $\rho \simeq 0.95$. Biasing led to a significant increase of the intermittence in the range $0.9 < \rho < 1$, peaking near $\rho \simeq 0.95$. We note that this position corresponds to the position of the 18/11 rational surface. This effect was similar at both the B and D probes.

In electron root conditions, biasing was such as to increase the potential and to enhance the positive radial electric field. Here, too, the larger absolute value of the radial electric field leads to an increased value of the intermittence parameter, and again the effect was similar at both probes.

Summarizing, in both conditions, the enhanced absolute value of the radial electric field leads to enhanced intermittence. This observation is consistent with the numerical results of Section 3 and the explanation in terms of the mixing between the temporal and spatial structure of the turbulence. Thus, the intermittence is both sensitive to the local magnetic configuration (the presence of rational surfaces [20]) and the radial electric field (or poloidal flow), as shown here, providing a window to improve our understanding of plasma turbulence. In future experiments, it could be attempted to apply a range of biasing voltages and vary the magnetic configuration (i.e., the radial placement of specific rational surfaces) in order to produce graphs like Fig. 3.

An interesting practical application may be the use of the intermittence parameter to determine the local rotation velocity state of the plasma. As observed, $C(1)$ achieves its deepest minimum when the local rotation velocity is small with respect to the laboratory frame of reference. If one therefore disposes of a means to vary the local rotation velocity, the point where the plasma rotation is halted with respect to the laboratory frame can be determined, and the turbulence spectrum or other quantities can then be obtained in the plasma frame of reference from a point measurement.

The intermittence may also be helpful when identifying the type of instability producing the fluctuations. In both conditions studied here (electron and in root),

biasing affected the intermittence to the same degree at both the B and D probes. The numerical model does not include the full geometry of TJ-II and hence cannot be used to compare differences or similarities between the probes. We note, however, that the field line curvature is rather different at the two probe locations. Namely, at probe B, the geodesic field line curvature is positive, whereas at probe D, it is negative. Likewise, normal field line curvature is negative but relatively small at probe B, and more strongly negative at probe D. As the intermittence response is similar, we speculate that the responsible instabilities are not curvature driven modes.

Acknowledgements

This work has been carried out within the framework of the EUROfusion Consortium, funded by the European Union via the Euratom Research and Training Programme (Grant Agreement No 101052200 – EUROfusion). Views and opinions expressed are however those of the author(s) only and do not necessarily reflect those of the European Union or the European Commission. Neither the European Union nor the European Commission can be held responsible for them. Research sponsored in part by the *Ministerio de Ciencia, Innovación y Universidades* of Spain under project Nos. PGC2018-097279-B-I00 and PID2019-110734RB-I00. B.A.C. gratefully acknowledges support for the research from the DOE office of Fusion Energy under U.S. Department of Energy Contract No. DE-SC0018076.

References

[1] C. D. Beidler, H. M. Smith, et al. "Demonstration of reduced neoclassical energy transport in Wendelstein 7-X". In: *Nature* 596.7871 (2021), pp. 221–226. DOI: 10.1038/s41586-021-03687-w.

[2] E. Ott. *Chaos in dynamical systems*. Cambridge, UK: Cambridge University Press, 1993. ISBN: 0 521 43215 4.

[3] B.B. Mandelbrot. *Multifractals and* $1/f$ *noise*. Springer, 1999. ISBN: 978-1461274346.

[4] B.A. Carreras, L. García, J.H. Nicolau, B.Ph. van Milligen, U. Hoefel, M. Hirsch, and the TJ-II and W7-X Teams. "Intermittence and turbulence in fusion devices". In: *Plasma Phys. Control. Fusion* 62 (2020), p. 025011. DOI: 10.1088/1361-6587/ab57f9.

[5] J.H. Harris, J.L. Cantrell, T.C. Hender, B.A. Carreras, and R.N. Morris. "A flexible heliac configuration". In: *Nucl. Fusion* 25.5 (1985), p. 623. DOI: 10.1088/0029-5515/25/5/005.

[6] C. Hidalgo, C. Alejaldre, et al. "Overview of TJ-II experiments". In: *Nucl. Fusion* 45 (2005), S266. DOI: 10.1088/0029-5515/45/10/S22.

[7] B.Ph. van Milligen, J. Hernández Nicolau, B. Liu, G. Grenfell, U. Losada, B. Carreras, L. García, and C. Hidalgo. "Filaments in the edge confinement region of TJ-II". In: *Nucl. Fusion* 58 (2018), p. 026030. DOI: 10.1088/1741-4326/aa9db6.

[8] C. Silva, B. Goncalves, M. A. Pedrosa, C. Hidalgo, K. McCarthy, E. Calderon, J. Herranz, I. Pastor, and O. Orozco. "Transport and fluctuations during electrode biasing on TJ-II". In: *Czech. J. Phys.* 55.12 (2005), p. 1589. DOI: 10.1007/s10582-006-0044-3.

[9] C. Meneveau and K.R. Sreenivasan. "Simple multifractal cascade model for fully developed turbulence". In: *Phys. Rev. Lett.* 59 (1987), p. 1424. DOI: 10.1103/PhysRevLett.59.1424.

[10] C. Meneveau and K.R. Sreenivasan. "The multifractal nature of turbulent energy dissipation". In: *J. Fluid Mechanics* 224 (1991), p. 429. DOI: 10.1017/S0022112091001830.

[11] B.A. Carreras, V.E. Lynch, D.E. Newman, R. Balbín, J. Bleuel, M.A. Pedrosa, M. Endler, B. van Milligen, E. Sánchez, and C. Hidalgo. "Intermittency of plasma edge fluctuation data: Multifractal analysis". In: *Phys. Plasmas* 7.8 (2000), p. 3278. DOI: 10.1063/1.874193.

[12] H.G.E. Hentschel and I. Procaccia. "The infinite number of generalized dimensions of fractals and strange attractors". In: *Physica D* 8.3 (1983), p. 435. DOI: 10.1016/0167-2789(83)90235-X.

[13] B. van Milligen, A. Melnikov, et al. "Topology of 2-D turbulent structures based on intermittence in the TJ-II stellarator". In: *Nucl. Fusion* 61.11 (2021), p. 116063. DOI: 10.1088/1741-4326/ac27c9.

[14] V.A. Sandborn. "Measurements of intermittency of turbulent motion in a boundary layer". In: *J. Fluid Mechanics* 6.2 (1959), p. 221. DOI: 10.1017/S0022112059000581.

[15] L. García, B.A. Carreras, V.E. Lynch, M.A. Pedrosa, and C. Hidalgo. "Sheared flow amplification by vacuum magnetic islands in stellarator plasmas". In: *Phys. Plasmas* 8.9 (2001), p. 4111. DOI: 10.1063/1.1392996.

[16] B.Ph. van Milligen, J.H. Nicolau, L. García, B.A. Carreras, C. Hidalgo, and the TJ-II Team. "The impact of rational surfaces on radial heat transport in TJ-II". In: *Nucl. Fusion* 57.5 (2017), p. 056028. DOI: 10.1088/1741-4326/aa611f.

[17] B.Ph. van Milligen, U. Hoefel, J.H. Nicolau, M. Hirsch, L. García, B.A. Carreras, C. Hidalgo, and the W7-X Team. "Study of radial heat transport in W7-X using the Transfer Entropy". In: *Nucl. Fusion* 58.7 (2018), p. 076002. DOI: 10.1088/1741-4326/aabf5d.

[18] H.R. Strauss. "Nonlinear, three-dimensional magnetohydrodynamics of noncircular tokamaks". In: *Phys. Fluids* 19 (1976), p. 134. DOI: 10.1063/1.861310.

[19] G. Grenfell, B.Ph. van Milligen, U. Losada, T. Wu, B. Liu, C. Silva, M. Spolaore, and C. Hidalgo. "Measurement and control of turbulence spreading in the Scrape-Off Layer of TJ-II". In: *Nucl. Fusion* 59 (2019), p. 016018. DOI: 10.1088/1741-4326/aaf034.

[20] B. Ph. van Milligen, B.A. Carreras, L. García, and C. Hidalgo. "The localization of low order rational surfaces based on the intermittence parameter in the TJ-II stellarator". In: *Nucl. Fusion* 60 (2020), p. 056010. DOI: 10.1088/1741-4326/ab79cc.